ACS APPLIED MATERIALS & INTERFACES

www.acsami.org Research Article

Hydrogen Behavior at Crystalline/Amorphous Interface of Transparent Oxide Semiconductor and Its Effects on Carrier Transport and Crystallization

Julia E. Medvedeva,* Kapil Sharma, Bishal Bhattarai, and Mariana I. Bertoni

Cite This: https://doi.org/10.1021/acsami.2c09604

Read Online

ACCESS | Metrics & More | Article Recommendations | Supporting Information

ABSTRACT: The role of disorder and particularly of the interfacial region between crystalline and amorphous phases of indium oxide in the formation of hydrogen defects with covalent (In−OH) or ionic (In−H−In) bonding are investigated using *ab initio* molecular dynamics and hybrid density-functional approaches. The results reveal that disorder stabilizes In−H−In defects even in the stoichiometric amorphous oxide and also promotes the formation of deep electron traps adjacent to In−OH defects. Furthermore, below-room-temperature fluctuations help switch interfacial In−H−In into In−OH, creating a new deep state in the process. This H-defect transformation limits not only the number of free carriers but also the grain size, as observed experimentally in heavily H-doped sputtered In_2O_x. On the other hand, the presence of In−OH helps break O_2 defects, abundant in the disordered indium oxide, and thus contributes to faster crystallization rates. The divergent electronic properties of the ionic vs covalent H defects—passivation of undercoordinated In atoms vs creation of new deep electron traps, respectively—and the different behavior of the two types of H defects during crystallization suggest that the resulting macroscopic properties of H-doped indium oxide are governed by the relative concentrations of the In−H−In and In−OH defects. The microscopic understanding of the H defect formation and properties developed in this work serves as a foundation for future research efforts to find ways to control H species during deposition.

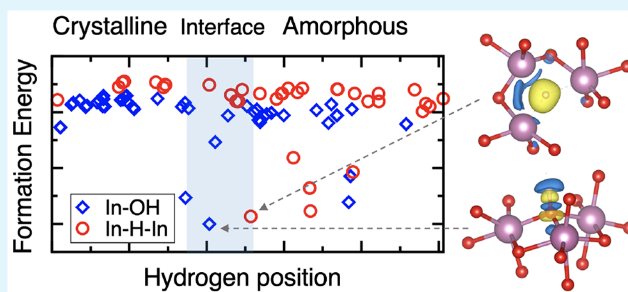

KEYWORDS: *wide-band-gap amorphous oxide semiconductors, hydrogen defects, crystalline/amorphous interfaces, ab initio molecular dynamics, density functional theory, carrier generation and transport, crystallization*

1. INTRODUCTION

Hydrogen has been known to play a key role in crystallization, defect passivation, doping, and improved transport properties in covalent semiconductors such as Si, although the properties of H defects in silicon are still under debate.[1] Revealing the microscopic behavior of hydrogen in wide-band-gap metal oxides that have been employed as transparent electrodes in many optoelectronic devices, including highly efficient silicon heterojunction solar cells, and that recently became competitive with silicon as an active transistor layer in large-area flexible displays,[2−10] represents a separate formidable problem. In oxides, hydrogen may passivate undercoordinated oxygen or metal atoms, forming covalent or ionic H bonds, respectively, and the resulting macroscopic properties depend on the relative formation, distribution, and behavior of the competing H defects.[11−17]

Although the structure and properties of substitutional and interstitial H defects in crystalline In_2O_3 have been studied theoretically,[18−23] the results cannot be transferred to the disordered phase. The ionic nature of metal−oxygen bonding renders a substantial disorder within the short-range structure of the amorphous oxide phases that feature large fractions of undecoordinated oxygen (O) and metal (M) atoms.[24−29] The wide coordination distributions and strong distortions in the M−O and O−M polyhedra dramatically increase the number of possible locations for hydrogen and the diversity of its immediate neighbor environment. The latter affects the formation, activation, and stability of various H defects as well as H mobility through the disordered structure. Therefore, accurate (quantum-mechanical) and statistically significant calculations are required to elucidate the complex H behavior in wide-band-gap amorphous oxide semiconductors.

It has been shown that H-doped crystalline indium oxide exhibits an excellent carrier mobility (>100 $cm^2/(V\ s)$) in combination with a tunable carrier density (10^{18}−10^{20} cm^{-3}) and optical transparency in the visible and near-infrared

Received: June 1, 2022
Accepted: August 12, 2022

Downloaded via MISSOURI UNIV SCIENCE & TECHNOLOGY on August 19, 2022 at 21:08:00 (UTC).
See https://pubs.acs.org/sharingguidelines for options on how to legitimately share published articles.

ACS Publications © XXXX American Chemical Society

regions, outperforming commercially employed tin-doped indium oxide (ITO).[30−33] H doping was shown to be responsible for a remarkable 70-fold increase in carrier mobility in amorphous In−Ga−O.[34] However, a recent observation of atypical semiconductor behavior in 7 atom % H-doped In_2O_{3-x} grown by sputtering, namely, the decreasing carrier concentration when temperature is increased from 50 to 300 K,[35] contradicts the widespread consensus that hydrogen is a shallow donor in In_2O_3 regardless of its crystallographic location (interstitial or substitutional) within the ordered oxide lattice.[18−20,22,23] In addition, the observed temperature-dependent electron mobility in In_2O_3 with variable H contents suggests that several carrier scattering mechanisms are simultaneously at play and that H partitioning or segregation is likely to occur.[35] To explain these puzzling observations, microscopic mechanisms of the formation and properties of H defects at the crystalline/amorphous In_2O_3 interface must be established.

Furthermore, the role of hydrogen in the crystallization of In_2O_3 has not been fully understood.[35−38] Although H doping leads to faster crystallization rates, there are contradictory reports regarding the grain size of the hydrogenated samples. On one hand, H-doped In_2O_3 films annealed at 250 °C exhibit larger grain sizes in comparison to the comparable films grown without hydrogen.[37] At the same time, systematic investigations have shown that the In_2O_3 grain size gradually decreases with increasing H content (from 0 to 3, 5, and 7 atom % H) in the samples grown by sputtering at room temperature and then annealing at 200 °C.[35] Studies of H-defect stability near the amorphous/crystalline interface may help determine H pinning and distribution at grain boundaries.

In this work, the formation, distribution, stability, and electronic properties of hydrogen defects within a crystalline/amorphous (c/a) In_2O_3 interface are studied using accurate hybrid density-functional calculations as implemented in VASP.[39−42] The interfacial models are built from crystalline and amorphous bulk; the latter was obtained via *ab initio* molecular dynamics liquid-quench simulations, and the structure has been experimentally validated in prior works.[26−29,43,44] For statistically significant results, the formation energy and bonding preferences of hydrogen in amorphous, interfacial, and crystalline regions are compared by placing a single H radical at 110 different locations in a 160-atom ($In_{64}O_{96}$) interface model followed by full structural optimization using the Perdew−Burke−Ernzerhof (PBE) exchange-correlation functional[45,46] and self-consistent hybrid-functional Heyd−Scuseria−Ernzerhof (HSE06) approach[47,48] for accurate electronic property calculations. To study the thermal stability of H defects, molecular dynamics simulations are performed at elevated temperatures: namely, at 100, 200, 300, 400, and 500 K. The specific details of the calculations and structural analysis are given in Section 4.

2. RESULTS AND DISCUSSION

2.1. Properties of the Hydrogen-Free c/a In_2O_3 Interface. First, the structural properties of an H-free stoichiometic fully relaxed c/a In_2O_3 interface were analyzed by calculating the first-shell effective coordination numbers (ECN) as well as In−O and O−In polyhedral distortions for each atom in the system (see Section 4 for details of the calculations). These characteristics highlight the differences between crystalline and amorphous regions in the interface: disorder reduces the average coordination and increases distortions in In−O and O−In polyhedra (Figure 1a,b), making the distributions much broader in comparison to those in the crystalline part of the interface (Figure 1c−f). A notable fraction of undercoordinated O (ECN ≈ 3) and In (ECN < 5) atoms is found at the interface and within the amorphous region (Figure 1c−f). The results are in agreement with prior reports for amorphous In_2O_3 bulk: namely, with the average effective coordination of In (O) being equal to 5.4 (3.6) and the average distortion of In−O (O−In) being equal to 0.0135 (0.0137).[26−29,43,44] This suggests that the c/a interface model adequately describes the amorphous oxide and also that the structural characteristics of the disordered oxide are attained within 1−2 atomic layers from the crystalline layer.

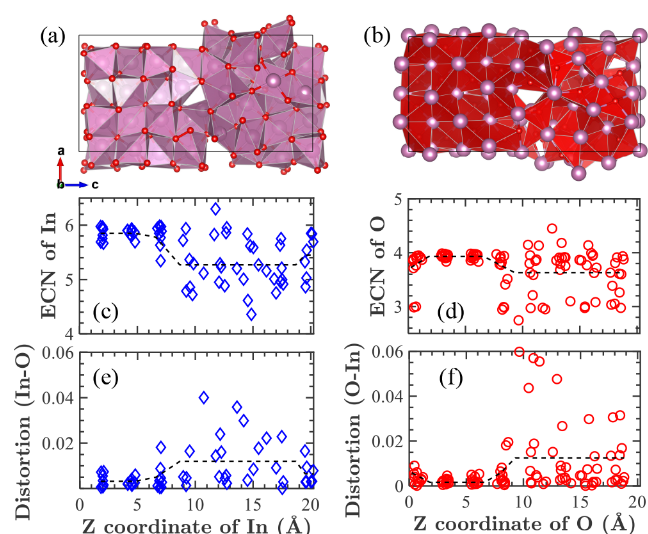

Figure 1. Atomic structure of the c/a In_2O_3 interface with In and O polyhedra shown in (a) and (b), respectively. The effective coordination numbers (ECN; see Section 4, (c) and (d), and polyhedral distortions, (e) and (f), calculated as a function of the *Z* coordinate of the In and O atoms, respectively. Dashed lines represent average values in different regions.

To determine the charge density distribution across the c/a interface, Bader charge contributions from individual In atoms to the conduction band (CB) bottom and from O atoms to the valence band (VB) top were calculated (Figure 2). The CB contributions from most of the In atoms located within the amorphous part are notably larger in comparison to those in the crystalline region (Figure 2a,c,e). Overall, the charge density distribution across the amorphous region is relatively uniform, with no charge accumulation at the interfaces (Figure 2c).

In marked contrast to In atoms, only six O atoms show significantly larger Bader contributions to the top of the VB in comparison to all other oxygen atoms (Figure 2b,d,f). All six O atoms are located near or at the interfaces between the crystalline and amorphous regions, forming three pairs with O−O distances of 2.8−3.0 Å, and five of them are 3-coordinated. Most importantly, all six localized O p orbitals are nearly perpendicular to the plane formed by the nearest neighbor In atoms (Figure 3a) and the charge localization is strongest when the two nonbonding O p orbitals align with each other, allowing for their direct overlap. At the same time, no two neighboring 3-coordinated O atoms abundant within the amorphous region (Figure 1d), arrange in similar mutually

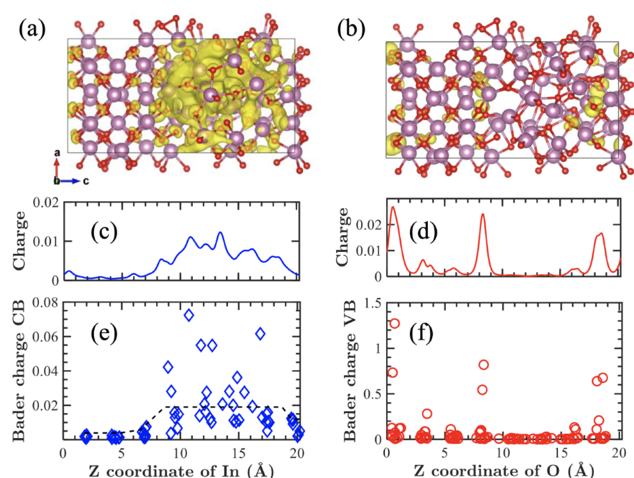

Figure 2. Charge density distribution calculated for the lowest-energy conduction band (a) and for the three highest-energy valence bands (b). Integrated charge density calculated as a projection to the z axis for the conduction (c) and valence bands (d). Bader charge contributions from In atoms to the conduction (e) and from O atoms to the valence bands (f). Inset in (f): a pair of localized O p orbitals oriented perpendicular to the plane formed by the nearest In atoms.

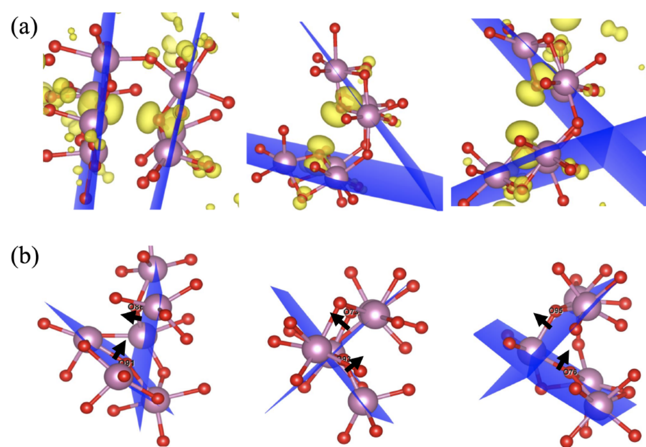

Figure 3. (a) Charge density distribution calculated within the top three occupied bands showing the localization at the six O p orbitals with the highest Bader charge contributions to these states, 28−35% of the total charge in one band per each O atom. The blue planes are constructed through the centers of the neighboring In atoms. (b) Atomic structures for pairs of 3-coordinated O atoms having an O−O distance of 2.8−3.0 Å, which is similar to the cases shown in (a). Black arrows show the direction normal to the plane drawn through the In neighbors. In these cases, the Bader charge contributions from the O atoms to the top three valence bands are below 0.5% of the total charge.

oriented planes of the In neighbors that would allow the p orbital alignment (Figure 3b). One can argue that the interfacial region with highly ordered In atoms on the crystalline side of the interface favors the formation of such defects. Nevertheless, the nonbonding O pairs that form strongly localized tail states at the top of the valence band were reported to be present in amorphous In−O and In−Ga−O bulk.[27,49] As will be shown below, these nonbonding O p orbitals attract hydrogen.

The band offset between crystalline and amorphous In_2O_3 phases is an important characteristic for device engineering as well as for an understanding of the charge transport within nanostructured In_2O_3 where both phases are present. It has been reported that disorder reduces the band gap of amorphous stoichiometric In_2O_3 bulk by 1 eV in comparison to bixbyite In_2O_3.[27] For the interfacial model, the band offset is estimated based on the projected electronic band structure calculations with contributions from the atoms in the crystalline and amorphous regions summed up separately. We find that the top of the valence band coincides for the crystalline and amorphous parts, whereas the conduction band is lower by 0.78 eV for the amorphous region than that for the crystalline region. This in accord with the CB charge density distribution across the interface (Figure 2a,c). We note here that the room-temperature equilibration with subsequent 0 K lattice relaxation of the c/a model appears to be sufficient to suppress structural defects that may cause charge accumulation at the stoichiometric interface.

The only interfacial defect that consistently appeared in the MD simulations is an O_2 defect with an O−O distance of 1.6 Å. It should be noted that the formation of O_2 defects has been reported to occur in bulk amorphous In_2O_3 and other ionic amorphous oxides.[27,29,50,51] Given the strong O−O bonding in the O_2 defect, especially in comparison to the weak ionic In−O bonding of the matrix, the peroxide is found to be stable up to 1100 K = 830 °C in our MD simulations. Therefore, the O_2 diffusion throughout the lattice during annealing and crystallization is limited and we do not expect segregation of O_2 defects at the c/a interface. This is supported by our MD simulations for the H-free c/a interface, which crystallizes at room temperature with the O_2 defect (see Section 2.6). At the same time, the abundant O_2 defects located in amorphous regions will become interfacial during crystal growth and may be broken apart by In−OH defects, as shown in Section 2.6.

For both c/a interfacial regions (formed due to periodic boundary conditions), the structural and electronic properties change within 2 Å, as is represented by the sloped parts of the dashed lines in Figures 1c−f and 2e. The narrow interfacial regions between crystalline and amorphous parts can be further illustrated using the partial vibrational density of states (VDOS) calculated for three different parts of the interface: namely, crystalline, amorphous, and interfacial regions (see Figure 13 in Section 4). The interfacial VDOS shows behavior intermediate to those of crystalline and amorphous regions with partially suppressed peaks, broadening, and a slight shift to the low-frequency modes, characteristic for an amorphous phase. Thus, we find that the structural, dynamic, and electronic properties reach their corresponding crystalline or amorphous bulk values within about 2 Å, making our choice of a 20 Å model sufficient to describe the c/a interface. The sharp c/a interface obtained in our calculations is in accord with the high-resolution TEM imaging of nanocrystallites in amorphous indium oxide.[52]

2.2. Properties of H Defects in c/a In_2O_3 Interface.

To study H distribution within the c/a interface, 110 random locations were identified throughout the structure so that the initial distance from H to its nearest neighbor was at least 1.6 Å. Each of the 110 structures with a single H radical placed into the initial location was fully relaxed with all atoms in the supercell allowed to move during the energy and atomic force minimization. The optimized H locations are shown simultaneously within the initial supercell in Figure 4a. Note that, during the relaxation, the positions for several H atoms converged to the same local minimum. Due to the structural

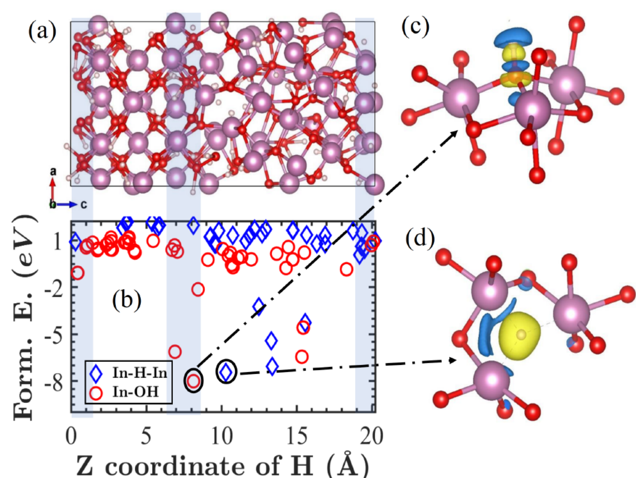

Figure 4. (a) 110 optimized H locations within the initial supercell shown simultaneously. (b) Formation energy as a function of the *Z* coordinate of H atoms. Light blue shading represents interfacial regions. (c, d) Charge transfer for the lowest-energy In−OH and In−H−In defects, respectively. The yellow (blue) isosurfaces represent positive (negative) charge density calculated as the charge difference with and without H.

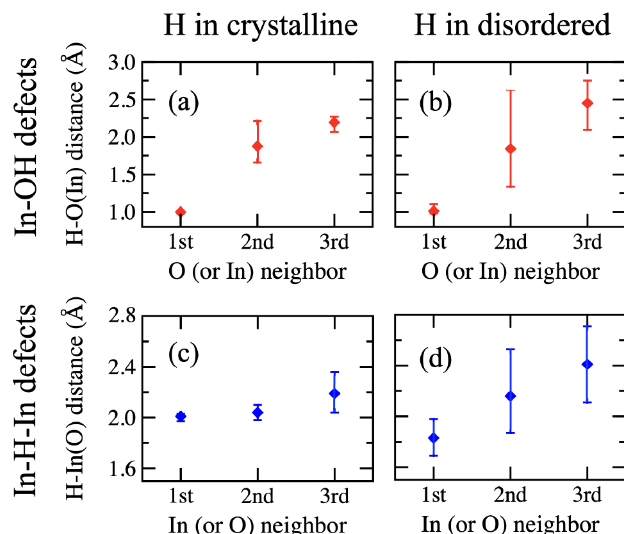

Figure 5. Calculated distances from the H atom to its nearest neighbors for (a, b) In−OH and (c, d) In−H−In defects located in (a, c) crystalline or (b, d) disordered regions of the c/a In_2O_3 interface. Diamond symbols represent the average values, and the lines show the distance ranges. For In−OH defects, the first and second nearest neighbors are always O atoms, whereas the third neighbor can be either an O or an In atom. For the In−H−In defects located in the crystalline part, the first three neighbors are always In atoms, whereas for the In−H−In defect located in the disordered regions, the second and/or third neighbor can be either an O atom or an In atom.

and electronic differences of individual atoms in the c/a interface (Figures 1 and 2), the energy of formation of H-doped structures, calculated as $E_{formation} = E(In_{64}O_{96}:H)_i - E(In_{64}O_{96}) - E(H_2)/2$, varies significantly for different H locations (Figure 4b). Based on the H nearest-neighbor environment, we identify two types of defects, In−OH and In−H−In. For the H defects in the crystalline part, the formation energy (+0.73 eV for In−OH and +2.01 eV for In−H−In) agrees well with previous works.[19,22] Among all H defects located in the disordered parts (interfaces and amorphous regions), 67% of In−OH and 13% of In−H−In have a negative formation energy. At the same time, both types of defects have several cases with a comparably low formation energy (Figure 4a). Further calculations of positively and negatively charged supercells show a similar trend in the formation energies of the charged H defects (see the Supporting Information).

2.2.1. In−OH Defects. From the total 110 cases of the hydrogenated c/a interface, 56 correspond to the formation of In−OH defects (Figure 4c). The O−H bond lengths for the OH defects located in the crystalline (17 cases) or disordered (39 cases) parts of the interface are similar, about 1.0 Å (Figure 5a,b). This implies that, regardless of the OH location in the c/a interface, hydrogen forms a strong covalent bond with sn O atom to become OH^-, as confirmed by the charge transfer plots (Figure 4c) and charged supercell calculations (see the Supporting Information). The results are also in agreement with previous reports.[49,53] Accordingly, for both crystalline and disordered regions, the OH states are located deep at the bottom of the valence band, about 8−10 eV below the Fermi level (see the Supporting Information).

Although the H distances to its nearest O atom are similar for all In−OH defects located in the crystalline and disordered regions, the proximity of the second O neighbor varies, especially in the latter case (Figure 5a,b). It has been shown that the distance from H to the second O neighbor determines the vibrational characteristics of the OH defects:[49] the shorter the distance, the lower the infrared frequency of the OH defect. In the case of the shortest distance from H to the second O neighbor (1.34 Å), hydrogen becomes trapped between the two oxygen nearest neighbors, forming an In−OH−O−In complex. This configuration limits the thermal motion of the OH bond—in contrast to the cases when the second O neighbor is far away (up to 2.63 Å) from H, so that the OH bond is free to rotate at high frequency with respect to the In−O bonds that form a “stationary” base in the In−OH defect. Importantly, we find that the average distances from H to the second O neighbor are 1.63 or 1.97 Å for the In−OH defects located in the interfacial or amorphous regions. This means that there is a higher probability to form In−OH−O−In complexes with trapped hydrogen either at or near the interface, likely due to the strong coordination mismatch of the In atoms that belong to the ordered and disordered sides of the interface.

Most strikingly, the formation of the covalent OH bond in the ordered or the disordered region has a different effect on the structure in the defect vicinity and also on the resulting electronic properties. An OH formed in the crystalline part weakens the In−O bonds in the In−OH defect: the average In−O bond length increases from 2.17 to 2.26 Å, in accord with the results of earlier works for H-doped crystalline In_2O_3 bulk.[19,22,49] Among the In−OH defects formed in the disordered regions, in addition to the In−O bond length elongation, we find that several In−O bonds are eliminated upon the OH formation. For example, in the H-doped structure with the lowest formation energy, one of the In−O distances increases by as much as 2.2 Å: namely, from 2.26 to 4.42 Å. In this case, the In atom displaced due to the OH formation not only loses one oxygen and becomes under-coordinated but also pairs with another low-coordinated In in its vicinity. The formation of a nonshared undercoordinated

https://doi.org/10.1021/acsami.2c09604
ACS Appl. Mater. Interfaces XXXX, XXX, XXX−XXX

In−In metallic bond with an In−In distance of 2.6−2.9 Å gives rise to a deep localized state within the band gap, at about −2.7 eV below the Fermi level, similar to an electron trap found in nonstoichiometric a-In_2O_{3-x} and related oxides.[27,28,54,55] Among the 110 H-doped cases considered (both In−OH and In−H−In defects), 6 cases form deep-gap states. All of them correspond to In−OH defect located in the disordered region (4 in the amorphous and 2 in the interfacial part), and all 6 cases have negative formation energy, 3 with $E_{formation}$ values below −6 eV and 3 with $E_{formation} \approx -0.6$ eV (Figure 4b). It should be noted that we find other cases of In−O bond breaking caused by the OH formation; however, the In atom bonds with another oxygen to compensate its unbalanced charge created by the covalent OH bonding, so that no deep defect state appears in the electronic structure. Thus, our results reveal that H doping is likely to introduce deep electron trap defects via energetically favorable OH formation which causes a subsequent structural bond rearrangement in the disordered oxide, enabling the In−In metallic bonding. The latter requires the presence of undercoordinated In atom(s) in its vicinity which, in turn, depends on the stoichiometry of the disordered oxide[27,28] and also on the ability of hydrogen to passivate the undercoordinated In atoms by forming competing In−H−In defects.[28]

2.2.2. In−H−In Defects. Nearly half (54) of the total 110 cases of H-doped c/a interface converged to an In−H−In defect, although only a few (13%) of the In−H−In located in the disordered parts of the stoichiometric interface show a negative formation energy. Unlike In−OH, the structural characteristics of In−H−In defects formed within the crystalline (8 cases) or disordered (46 cases) regions differ significantly. In the crystalline oxide, H is nearly equidistant from its first 2 (and in some cases, 3) In nearest neighbors (Figure 5c). For the In−H−In defects in the disordered regions, the average nearest-neighbor In−H distance is considerably shorter (1.83 Å) in comparison to that for the H defects in the crystalline region (2.01 Å). Importantly, the shortest In−H distance of 1.68 Å is still above the typical In−H bond length in indium hydride (1.63 Å), suggesting a weak In−H bonding in the oxide. The second and third neighbors of H not only are found at shorter or much longer distances in comparison to the crystalline oxide (cf. Figure 5(cd) but also may be either In or O atoms. Specifically, 28% of the second and 85% of the third neighbors of H are oxygen atoms, resulting in the formation of 1 (28%)-, 2 (59%)- or 3-coordinated (13%) hydrogens surrounded with In atoms—in marked contrast to the crystalline region, where all H defects are 3-coordinated with In. Despite the low occurrence, 4 In−H−In defects with the lowest formation energy, with an $E_{formation}$ value below −5 eV (Figure 4b), correspond to the three-coordinated H (Figure 4d). The asymmetry of the H neighbor environment originates from the low In coordination and/or strong distortions of the In−O polyhedra in the disordered part of the interface (Figure 1c,e). It reduces the H defect formation energy in compared to those in the crystalline In_2O_3 (Figure 4b).

The formation of In−H−In defects reduces the effective coordination of participating In atoms from 5.85 (5.22) to 5.73 (4.97) for the H defects located in the crystalline (disordered) regions. Weakening of the In−O bonding signifies that hydrogen gains an additional electron from the neighboring In atoms to become H^- and to form ionic bond(s), as confirmed by the charge transfer analysis (Figure 4d), charged supercell calculations (see the Supporting Information), and the calculated Bader charge. Due to the short nearest-neighbor H−In distances for the In−H−In defects located in the disordered regions (Figure 5c,d), the In−H hybridization leads to the formation of bonding/antibonding H states that contribute to the valence/conduction bands, respectively—in marked contrast to the strongly localized H states formed within the band gap, at about −1.9 eV below the Fermi level, for the In−H−In defects in the crystalline region of the interface (see the Supporting Information).

Note that the formation of In−H−In defects in highly nonstoichiometric amorphous indium oxide has been investigated previously.[28] It was shown that H passivation of undercoordinated In atoms leads to compensation of the strongly localized O defect states, enhancing both the number of free carriers and the carrier mobility. The results of the current work reveal that there is a second, competing mechanism of defect formation in H-doped disordered oxides, and the overall electronic properties depend on the balance between the number of defects with ionic and covalent H bonding.

2.3. Hydrogen Passivation of Undercoordinated In or O vs Bond Reconfiguration. Hydrogen passivation of dangling bonds arising from undercoordinated Si atoms is one of the major reasons for the improved properties of amorphous Si. In wide-band-gap oxide semiconductors, the role of hydrogen is more complex. For In−OH defects, we find that neither the low coordination of oxygen (Figure 1d) nor the nonbonding oxygen tail states (Figure 2b,d,f) determine the defect formation in amorphous indium oxide. The average formation energy of the OH defects formed with 3-coordinated O atoms (22 cases, ECN = 2.9−3.2), −0.78 eV, is slightly higher than that for the 4-coordinated O atoms (17 cases, ECN = 3.6−4.5), −1.05 eV. Similar formation energies (−0.9, −1.1, and −2.1 eV) are obtained for the structures where hydrogen passivates one of the three strongly localized O p orbital pairs (Figure 2b,d,f). The four lowest-energy cases with In−OH defects, i.e., those with a formation energy below −5 eV (Figure 4b), do not show a preference for a 3-coordinated O atom.

Similarly, the formation energy of In−H−In defects in the stoichiometric c/a In_2O_3 interface does not appear to correlate with the initial (prior to H doping) coordination of In atoms or the resulting nearest-neighbor In−H distance. (In highly nonstoichiometric amorphous indium oxide, hydrogen was found to effectively passivate the oxygen defects formed by clusters of two or more undercoordinated, undershared In atoms.[28])

A further analysis reveals that both covalent and ionic H bonding reduces the coordination of the nearest neighbors of H to as low as 2.0 for O in In−OH and 3.4 for In in the In−H−In defects in some of the low-energy cases. The H-induced coordination reduction causes a ripple effect on the structure well beyond the nearest neighbors of H. The long-range effect of H doping on the structural rearrangement can be seen from infrared (IR) calculations. Both types of H defects lead to significant changes within the IR spectrum of the oxide lattice itself: i.e., within the range from 20 to 700 cm^{-1} (see Figure 13 in Section 4. Similar results were recently reported for H-doped amorphous In−Ga−O, where changes in the coordination and polyhedral distortions were found to occur for the In and Ga atoms located as far away from H defects as 9 Å.[49]

https://doi.org/10.1021/acsami.2c09604
ACS Appl. Mater. Interfaces XXXX, XXX, XXX−XXX

The structural reconfiguration can be quantified by comparing the formation energy of the fully relaxed structures (Figure 4b) to that obtained using constrained relaxation when only the H position is optimized in an otherwise fixed lattice (Figure 6a). In the latter approach, a negative formation energy is found only for the H passivation of one of the six strongly localized O p orbitals (Figures 2b,d,f), whereas In−H−In defects not only are scarce but also have a notably higher formation energy in comparison to that for the In−OH cases (Figure 6a). This implies that structural relaxation (i) lowers the energy of some cases by as much as 8 eV, (ii) outweighs the energy gains of H passivation of the nonbonding O tail states, and (iii) favors the formation of In−H−In defects in the stoichiometric disordered oxide.

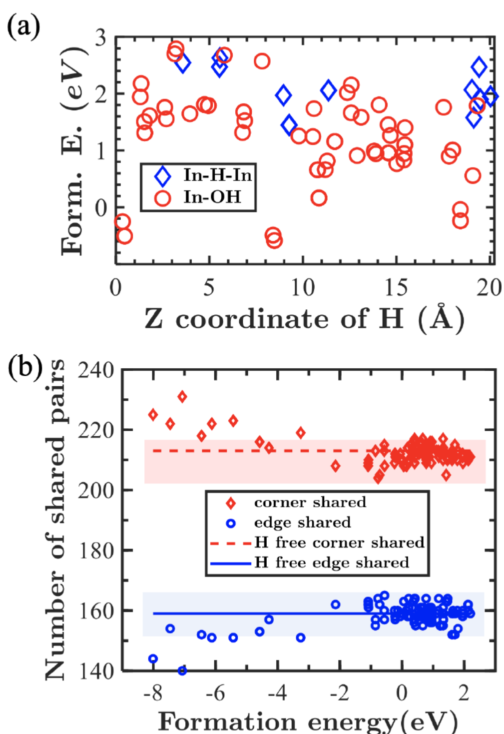

Figure 6. (a) Formation energy of the 110 cases of an H-doped c/a In_2O_3 interface with constrained relaxation when only the H position is optimized in an otherwise fixed lattice. (b) Total number of edge- and corner-shared In−In pairs for 110 fully relaxed cases as a function of the corresponding formation energy, shown in Figure 4b. Dashed lines represent the corresponding values for the H-free case; shaded areas highlight the ranges for the majority of cases with higher formation energy.

To further quantify the effect of H doping on the structural rearrangement in the c/a In_2O_3 interface, we calculated the number of edge- and corner-shared In−In pairs in the fully relaxed structures before and after H doping and plotted the results as a function of the H defect formation energy for all 110 cases (Figure 6b). The number of corner-shared pairs is found to be notably larger for several low-energy cases in comparison to all other H-doped cases. The increased number of corner-shared polyhedra has been associated with better mobility in amorphous In_2O_3.[26,29,43,56] Indeed, in the In−H−In case that has the largest number of corner-shared pairs (232), the calculated conduction bandwidth is 1.79 eV, which is considerably larger than that in the H-free case, 1.67 eV. The CB width determines the free electron velocity; hence, it governs the free carrier mobility.[28,29] This is in accord with the improved electron mobility upon H doping of amorphous indium oxide[35−37] and of amorphous In−Ga−O.[34]

2.4. Thermal Stability of Hydrogen Defects. To study the thermal stability of the energetically favorable H defects and to understand their role during crystallization, we performed molecular dynamics simulations at elevated temperatures, from 100 to 500 K. For this, the following structures were chosen: (i) the In−OH and In−H−In defects that correspond to the lowest formation energy (both defects are in the disordered region), (ii) the In−OH defect located in the crystalline region, and (iii) one of the low-energy In−H−In defects located in the amorphous region. For comparison, MD simulations were also performed for an H-free interface.

We find that the lowest-energy In−H−In defect ($E_{formation}$ = −7.5 eV) that is closest to the c/a interface among the five low-energy In−H−In defects (Figure 4b) is stable at 100 and 200 K: i.e., hydrogen maintains the average distance to its three In nearest neighbors as well as to the fourth neighbor, an oxygen atom (Figure 7a). However, room-temperature fluctuations break the ionic H bonds of this defect so that hydrogen moves away, gets captured by its oxygen neighbor, and forms a stable covalent OH bond at the interface (Figures 7a and 8). Importantly, the two undercoordinated In atoms that the hydrogen leaves behind move closer together, creating an undershared pair with an In−In distance of 2.67 Å. This is facilitated by the In−OH formation that weakens the In−O bonds in the defect, resulting in a lack of available oxygen for the nearby In atoms. As a result, the shallow state associated with the interfacial In−H−In defect (Figure 8a) changes to a deep electron trap at −2.6 eV below the Fermi level (Figure 8b), located at the interface. Hence, in addition to the energetically favorable OH-induced deep traps found at 0 K relaxation (see Section 2.2), moderate temperature will increase the number of in-gap defect states due to switching of the interfacial In−H−In defects into In−OH.

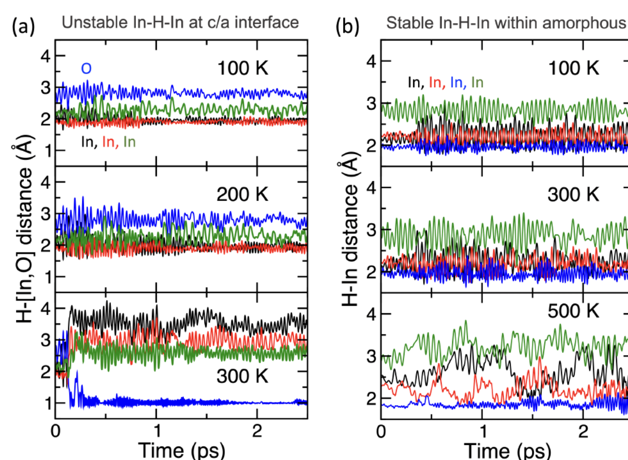

Figure 7. Calculated distance from H to its nearest neighbors at elevated temperatures as a function of time for two In−H−In defects. (a) The initial structure that at 0 K corresponds to the lowest-energy In−H−In defect located near the c/a interface, with an $E_{formation}$ value below −7.5 eV (Figure 4b). (b) The initial structure that at 0 K corresponds to one of the low-energy In−H−In defects located within the amorphous region of the c/a interface, with an $E_{formation}$ value below −5.5 eV (Figure 4b).

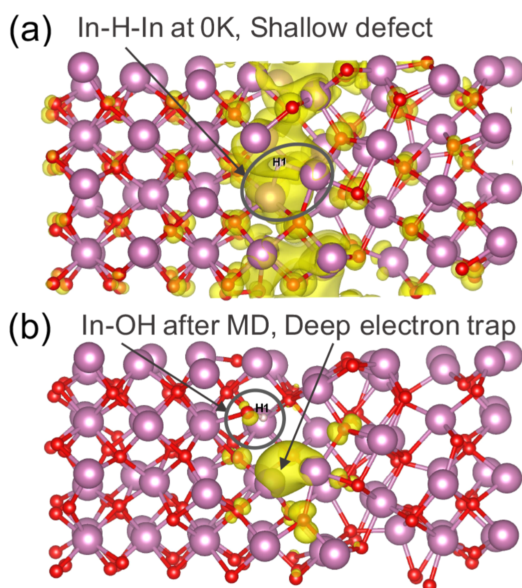

Figure 8. (a) Charge density distribution in the conduction band of the lowest-energy structure with an In−H−In defect located at the c/a interface. The defect is part of a shallow state that accumulates charge at the interface. (b) Charge density distribution for the strongly localized state located inside the band gap at −2.6 eV below the Fermi level and associated with ab undershared, undercoordinated In−In pair created upon switching of the interfacial In−H−In into an In−OH defect after the structure from (a) was heated to 300 K and then cooled back to 0 K.

To determine whether the unstable behavior of the interfacial In−H−In defect is common to that of In−H−In in an amorphous region, we performed MD simulations for the In−H−In defect that resides within the amorphous region away from the interface and has a low formation energy ($E_{formation}$ = −5.5 eV). In marked contrast to the interfacial In−H−In defect, the hydrogen in the amorphous part maintains the average distance to its nearest In neighbors even at 500 K (Figure 7b). The thermal stability of amorphous In−H−In defects can be explained by the large fraction of under-coordinated highly distorted In atoms in this region (Figure 1c). Being shared between three or four undercoordinated In atoms, hydrogen becomes effectively trapped in three dimensions. In contrast, the narrow interfacial region consists of fully coordinated In atoms on the crystalline side and undercoordinated In on the amorphous side of the interface (Figure 1c). The constraint not only limits the number of undercoordinated In neighbors for H but also allows H to escape. Indeed, at low temperatures, the interfacial In−H−In defect becomes essentially two-coordinated with the third In being farther away (Figure 7a), whereas the In−H−In defect in the amorphous region remains 3-coordinated with the three In−H distances being similar at low temperature (Figure 7b). At high temperature, it becomes an In−H defect with H bonded to a single In atom (Figure 7b). The behavior of the interfacial In−H−In caused by an In coordination mismatch is analogous to the thermally unstable In−H−Ga defects found in amorphous In−Ga−O bulk in comparison to the In−H−In and Ga−H−Ga defects.[49]

2.5. Atypical Semiconductor Behavior in H-Doped Indium Oxide. The switching of interfacial In−H−In defects into In−OH at temperatures at or below 300 K (Figure 7a) explains the puzzling observation of atypical semiconductor behavior in sputtered 7 atom % H-doped indium oxide annealed at 200 °C: namely, the decreasing carrier concentration when the temperature is increased from 50 to 300 K.[35] Because thermal fluctuations facilitate switching of interfacial In−H−In defects into In−OH (see Section 2.4), the resulting formation of deep electron traps (Figure 8b) reduces the number of free carriers when the temperature is increased. Importantly, the unusual temperature dependence of the carrier concentration is observed only in the annealed highly-H-doped indium oxide samples, where the grain sizes were found to be the smallest among the 0, 3, 5, and 7 atom % H-doped indium oxide samples. Therefore, the fraction of the interfacial c/a regions is the greatest in the films with the highest H content. Moreover, the 7 atom % H-doped samples exhibit the largest oxygen substoichiometry (i.e., the lowest oxygen content[35]); therefore, one should expect the largest fraction of the In−H−In defects in these samples, because hydrogen tends to passivate the abundant undercoordinated In atoms.[28] The combination of a large fraction of the c/a interfacial region with abundant In−H−In defects in the disordered parts implies that the concentration of interfacial In−H−In defects should be largest in this case. When the temperature is increased, the unstable interfacial In−H−In defects give away hydrogen that forms a stronger covalent bond with an oxygen, whereas the released electrons are trapped at a newly created undercoordinated, undershared In−In pair, having a pronounced effect on the carrier concentration.

2.6. Role of H Defects in Crystallization. The above MD results also suggest that the formation of interfacial deep trap states enabled by In−H−In to In−OH defect switching impedes crystallization even at elevated temperatures (400 K). Longer MD simulations for the configuration with the interfacial In−OH coupled with a deep trap state (Figure 8b) reveal that the structure does not fully crystallize within 120 ps at 300 K (Figure 9a,d) and within at least 50 ps at 400 K. For comparison, an H-free interface crystallizes after about 12 ps at 300 K (Figure 9a,b). Most strikingly, the fastest crystallization, within 2.5 ps at 300 K, is obtained for the structure that has an In−OH defect in the crystalline region: the presence of the In−OH helps break an interfacial O_2 defect (Figure 9a,c). Isolated O_2 defects were shown to be stable up to 1100 K in amorphous H-free In_2O_3 bulk.[27] Therefore, we find two competing mechanisms to explain the controversial experimental observations of a faster crystallization rate in H-doped indium oxide yet smaller grain sizes with increasing H concentration.[35] On one hand, stable In−OH defects located in the crystalline region help break an interfacial O_2 by weakening the In−O bond in the defect and, as a result, requiring the In atom(s) to seek for additional oxygen in the vicinity. The O_2 breaking releases two oxygen atoms, helping In neighbors attain the desired octahedral coordination. This leads to a faster crystallization in comparison to an H-free interface with a O_2 defect. At the same time, during crystallization, the expanding interfacial region encounters In−H−In defects, abundant in the amorphous oxide, facilitating the switch to In−OH that is accompanied by a deep trap oxygen defect. We find that, unlike an isolated oxygen vacancy (Figure 9b), an O defect coupled with interstitial In−OH impedes further crystal growth.

The above MD results suggest that there are at least two competing mechanisms that may affect crystallization: (i) switching of an interfacial In−H−In defect into In−OH with

https://doi.org/10.1021/acsami.2c09604
ACS Appl. Mater. Interfaces XXXX, XXX, XXX−XXX

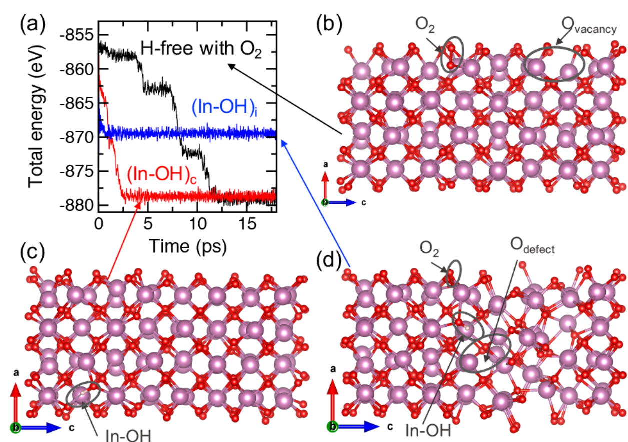

Figure 9. Room-temperature MD simulations for crystallization of H-free and H-doped c/a interfaces. (a) Calculated total energy as a function of time for three different structures described below. (b) Hydrogen-free c/a interfaces that crystallized with an O_2 defect and an oxygen vacancy (a Frenkel pair). (c) A crystallized structure with an In−OH defect and no O_2 defect. The initial 0 K structure possessed an In−OH defect in the crystalline region and an O_2 defect at the interface. (d) A structure that is not fully crystallized, showing an O_2, In−OH, and deep trap oxygen defect, all located near the interfacial region. Prior to MD simulations, this configuration corresponds to the lowest-energy In−H−In defect located near the c/a interface; the In−H−In defect is converted to In−OH at 300 K after 0.2 ps (Figure 7a).

the subsequent formation of a bound oxygen defect that prevents crystal growth and (ii) In−OH formation that helps break a nearby O_2 defect, promoting faster crystallization. It must be stressed that the oxygen stoichiometry, cation composition, or density of amorphous indium oxide may influence the formation and concentration of stable In−OH, In−H−In, and O_2 defects and, hence, is likely to affect both the crystal grain size and the crystallization rate, explaining a wide variety of experimental observations reported in the literature. In addition, the film thickness and density and the oxygen environment during annealing are important control parameters of the crystallization process.[52,57] To address the effects of those parameters computationally, models of an amorphous oxide surface or a slab would be required in order to properly simulate surface defects, oxygen adsorption, diffusion, and defect passivation.

Because interfacial In−H−In defects are found to be unstable and have a strong tendency to switch to In−OH at elevated temperature during crystallization, the majority of stable In−H−In defects are expected to reside within disordered and/or oxygen-deficient parts of the structure: e.g., at grain boundaries. The balance between In−OH and In−H−In defects will determine the resulting electronic properties of the material.

It should be noted that the critical role of OH defects in the crystallization of indium oxide may explain a contradictory observation that a lack of water increases crystallization in In_2Se_3.[58] The differences in crystallization dynamics in hydrogenated selenide and oxide are likely to stem from the different bond strengths between hydrogen and the anion: the H−Se bond (276 kJ/mol) is significantly weaker in comparison to the H−O bond (459 kJ/mol) and, therefore, covalent H bonding with an anion is less likely in amorphous In_2Se_3, resulting in a larger fraction of ionic In−H−In defects in hydrogenated selenide.

Finally, we stress that the current work represents a microscopic picture of possible H defects and H-induced atomic-scale structural transformations within a picosecond time frame that may either trigger or hinder the crystallization processes on a larger scale. To tackle a macroscopic description of crystallization kinetics and time evolution,[52] one would require a larger-scale computational approach: e.g., phase-field modeling.

3. CONCLUSION

In summary, *ab initio* investigations of an H-doped crystalline/amorphous In_2O_3 interface highlight the complex, dual nature of hydrogen defects in the wide-band-gap oxide semiconductor. The formation of ionic or covalent H bonds and the structural, thermal, and electronic properties of the H defects strongly depend on the defect location within the interface. This finding underscores the important role of the amorphous−crystalline nanostructure[43] and grain boundaries in the resulting macroscopic properties of metal oxides.

The results reveal that the extended structural rearrangement induced in the disordered oxide by H doping is the reason for (i) the low formation energy of In−OH defects in the amorphous and interfacial regions that outweighs the energy gains from H passivation of 3-coordinated O atoms and nonbonding O p orbitals, (ii) partitioning and thermal stability of In−H−In defects in the amorphous stoichiometric oxide, and (iii) an improved corner-shared polyhedral morphology that leads to a wider conduction band and increased electron velocity and, hence, enhanced carrier mobility in H-doped indium oxide.

Furthermore, our systematic, statistically significant investigations of H doping in the crystalline/amorphous interface help explain several puzzling or controversial experimental observations, including the following.

(1) Faster crystallization at room (or elevated) temperature in H-doped indium oxide due to the In−OH formation that breaks an interfacial O_2 defect releases the two oxygen atoms that help In neighbors attain the desired octahedral coordination.

(2) Despite faster crystallization rates due to H-doping, the formation of deep trap states coupled to covalent-bonded In−OH that arises from unstable interfacial In−H−In defects as well as interfacial H pinning due to formation of In−OH−O−In complexes impede crystal growth—in accord with the observed decreasing grain sizes as the H concentration increases in sputtered indium oxide.[35]

(3) Decreasing carrier concentration is due to thermally unstable interfacial In−H−In defects that, at moderate temperatures, switch to In−OH and create a deep electron trap, limiting the number of free carriers—in accord with puzzling experimental observations of the decreasing number of free electrons when temperature is increased from 50 to 300 K in sputtered indium oxide doped with 7 atom % H.[35]

(4) In marked contrast to a widespread understanding that H addition helps passivate oxygen defects in indium oxide (which was recently confirmed via systematic theoretical investigations of highly nonstoichiometric indium oxide[28]), the results of this work reveal two

https://doi.org/10.1021/acsami.2c09604
ACS Appl. Mater. Interfaces XXXX, XXX, XXX−XXX

competing mechanisms that promote deep traps in H-doped indium oxide—the formation of energetically favorable In−OH defects in the disordered oxide and thermal switching of the interfacial In−H−In into In−OH coupled with an O defect. Similar to the deep trap states caused by oxygen nonstoichiometry,[27,28] the H-induced O defects will be sensitive to photoillumination and are expected to contribute to the observed negative bias illumination stress (NBIS) instability behavior in thin-film transistor devices, one of the major drawbacks hampering commercialization of the amorphous oxide semiconductors. Therefore, the results of this work serve as a foundation for further investigations of the observed persistent photoconductivity and instability under illumination of H-doped indium oxide.

4. THEORETICAL METHODS AND APPROXIMATIONS

Prior to the construction of the crystalline/amorphous (c/a) interface, an amorphous bulk In_2O_3 structure was obtained using an *ab initio* molecular dynamics (MD) liquid-quench approach as implemented in the Vienna *ab initio* Simulation Package (VASP).[39−42] The calculations are based on density functional theory (DFT) with periodic boundary conditions[59,60] and employ the Perdew−Burke−Ernzerhof (PBE) exchange-correlation functional[45,46] within the projector augmented-wave method.[61,62] An 80-atom bixbyite cell of In_2O_3 was used as the initial structure, which was melted at 3000 K to eliminate any crystalline memory and to randomize the structure. The density of the amorphous structure was initially set to 7.12 g/cm^3 and subsequently optimized in accordance with earlier investigations.[27,29] Next, liquid-quench simulations were performed as follows. The quenched structure was cooled to 2500 K at an MD rate of 100 K/ps and then rapidly quenched to 100 K at a 200 K/ps rate. An energy cutoff of 260 eV and a single Γ-point method were used during melting and quenching processes. The structure was equilibrated at 300 K for 6 ps with a cutoff energy of 400 eV. Figure 10 shows a

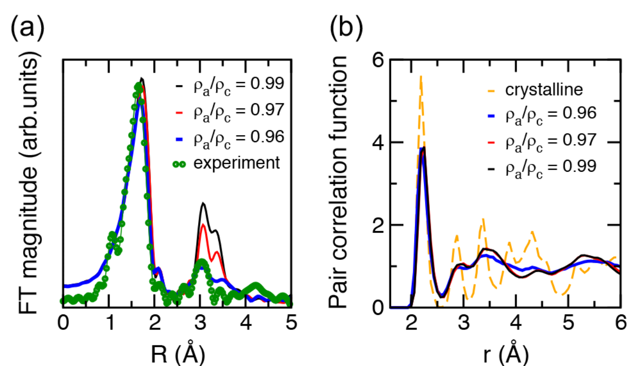

Figure 10. (a) Calculated and experimentally measured EXAFS spectra for MD-simulated and PLD-grown amorphous indium oxide bulk. (b) Calculated pair distribution function for crystalline and amorphous indium oxide bulk with different densities.

direct comparison between the extended X-ray absorption fine structure (EXAFS) spectra calculated based on the MD-simulated structures for amorphous indium oxide and the available experimental measurements.[29] The excellent agreement between the experimental and theoretical curves in the first and second EXAFS peaks that represent the first-, second-, and third-shell structure in indium oxide validates our MD liquid-quench models for amorphous indium oxide bulk.

Next, the 80-atom crystalline (bixbyite) and the room-temperature equilibrated amorphous bulk In_2O_3 structures were merged along the *z* axis (Figure 11). To reduce the interfacial strain in the resulting 160-atom model, MD equilibration cycles were performed at 300 K

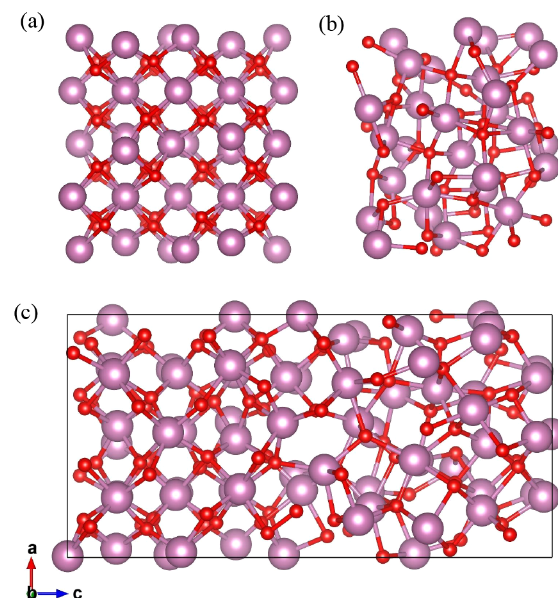

Figure 11. (a) 80-atom cubic cell for the crystalline In_2O_3 structure. (b) 80-atom cubic cell for amorphous In_2O_3. (c) 160-atom supercell for In_2O_3 formed by merging crystalline and amorphous bulk structures along the *z* axis followed by MD equilibration at 300 K for 30 ps.

for 30 ps. By an analysis of the total energy behavior at room temperature for the final 1000 MD steps of the equilibration run, the c/a interfacial model was found to correspond to a stable solution with no energy drift and small thermal fluctuations in the total energy that represent a structure in equilibrium. In addition, we performed lattice relaxation within DFT using the PBE functional at 0 K to minimize lattice strain in the interfacial regions. During the relaxation, a cutoff energy of 500 eV and a Γ-centered 8-*k*-point mesh were used; the atomic positions were relaxed until the Hellmann−Feynman force on each atom was below 0.01 eV/Å.

It is important to note that the room-temperature equilibration with subsequent lattice relaxation are sufficient to reduce charge accumulation at the H-free c/a interface, as discussed in Section 2.1. Furthermore, the c/a model is assessed (i) by analyzing the structural properties of individual In and O atoms as a function of their distance from the interface, (ii) by calculating the charge density distribution and the vibrational and electronic density of states for the crystalline, interfacial, and amorphous regions, and (iii) by comparing the results to the corresponding values for the crystalline or amorphous bulk. We find that distance distributions of the H-free c/a interfacial model do not exhibit strain for the atoms in the interfacial region: e.g., shorter or longer bonds or stronger distortion than that in the bulk. This is in accord with no charge accumulation at the interface, no negative vibrational modes, and no in-gap electronic states that could have pointed out an existence of strain at the interface. Both the vibrational and electronic densities of states change gradually from a crystalline to an amorphous region, as discussed in Section 2.1.

To accurately determine the distribution of hydrogen within the c/a interface, a single H radical was placed at 110 locations throughout the structure so that the initial distance from H to its nearest neighbor was at least 1.6 Å. Each configuration was then optimized within DFT using the PBE functional. For the optimization, a cutoff energy of 500 eV and a Γ-centered 8-*k*-point mesh were used; the atomic positions were relaxed until the Hellmann−Feynman force on each atom was below 0.01 eV/Å. The formation energy was calculated based on the total energy obtained for H-restricted relaxed (only the H position was optimized, while the atoms in the lattice were fixed) or fully relaxed (all atoms were allowed to move during optimization) structures according to the equation

https://doi.org/10.1021/acsami.2c09604
ACS Appl. Mater. Interfaces XXXX, XXX, XXX−XXX

$$E^{i}_{\text{formation}} = E(\text{In}_{64}\text{O}_{96}\text{:H})_i - E(\text{In}_{64}\text{O}_{96}) - E(\text{H}_2)/2 \quad (4.1)$$

where $E(In_{64}O_{96}:H)_i$ is the total energy of am H-doped supercell with an ith position of H, $E(In_{64}O_{96})$ is the total energy of the supercell before H doping, and $E(H_2)/2$ is half of the total energy of an H_2 molecule, which is also equivalent to the chemical potential of hydrogen.

To analyze the structural peculiarities of crystalline, amorphous, and interfacial regions in H-free and H-doped stoichiometric models, the average effective first-shell In−O distance for each In−O polyhedron was calculated according to[63]

$$l_{\text{av}} = \frac{\sum_i l_i \exp\left[1 - \left(\frac{l_i}{l_{\min}}\right)^6\right]}{\sum_i \exp\left[1 - \left(\frac{l_i}{l_{\min}}\right)^6\right]} \quad (4.2)$$

where the summation runs over all oxygen neighbors of a particular metal atom and l_{min} is the shortest In−O distance in the given In−O polyhedron. Next, the first-shell effective coordination number (ECN) for each atom was calculated according to

$$\text{ECN} = \sum_i \exp\left[1 - \left(\frac{l_i}{l_{\text{av}}}\right)^6\right] \quad (4.3)$$

In addition, we calculate the distortion of each In−O polyhedron, σ^2, characterized by the standard deviation of the individual In−O bond length (l_i) from the average In−O bond length (l_{av}) for the given polyhedron.

The electronic properties of several PBE-optimized supercell structures with and without H doping were calculated using the self-consistent hybrid-functional Heyd−Scuseria−Ernzerhof (HSE06) approach[48] with a mixing parameter of 0.25 and a screening parameter α of 0.2 Å^{-1}. For these computationally expensive calculations, H-free and 10 H-doped cases (4 In−OH and 4 In−H−In lowest-energy structures with an H defect located in the disordered part as well as In−OH and In−H−In structures with an H defect in the crystalline part) were selected. Next, the electronic band structure, density of states, and charge density distributions were calculated. The projected density of states calculated for the atoms in the crystalline or amorphous parts of the stoichiometric In_2O_3 interface is given in Figure 12.

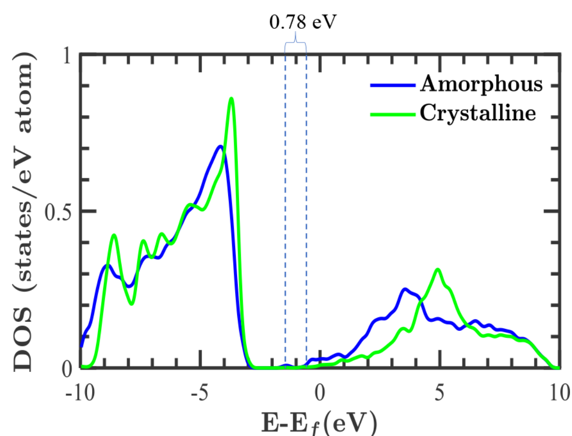

Figure 12. Projected density of states calculated for the atoms in the crystalline (green) and amorphous (blue) parts of the stoichiometric In_2O_3 interface. The band offset determined based on the projected electronic band structure is shown with dotted vertical lines. Note that the H-free stoichiometric c/a interface shows conducting behavior due to the presence of a O_2 defect that is found to be common at c/a interfaces.

To quantify the localization of the electronic states, the inverse participation ratio (IPR) of an orbital $\Psi_n(\vec{r}_i)$ was found from *ab initio* density-functional calculations according to the equation

$$\text{IPR}(\Psi_n) = N\frac{\sum_{i=1}^{N} |\Psi_n(\vec{r}_i)|^4}{\left|\sum_{i=1}^{N} |\Psi_n(\vec{r}_i)|^2\right|^2} \quad (4.4)$$

where N is the number of volume elements in the cell and i is the index of the volume element. An IPR value of 1 corresponds to a delocalized state with equal atomic orbital contributions from all atoms in the system. Conversely, the higher the IPR value, the stronger the localization of the given state.

To analyze the charge contributions from the states of individual atoms, a Bader charge was calculated for each atom[64] for the valence and conduction states. These calculations are based on the charge density distribution gradient and hence provide a much more accurate description of the electron localization in disordered oxide materials in comparison to the traditional electronic structure tools such as atom-resolved density of states calculations that rely on a fixed cutoff radius around atoms. Accurate Bader charge calculations are especially critical in disordered ionic oxides, where the charge distribution is likely to be nonspherical near low-coordinated atoms with strong distortions in the first shell. The PBE-optimized atomic structures and HSE06-calculated charge densities were plotted using VESTA software.[65]

The vibrational density of states (VDOS) provides key information about the local bonding environment and gives an accurate assessment of the dynamical stability of the structure. To obtain the VDOS, dynamic calculations were carried out using VASP with stringent convergence criteria for force and energy minimization. In the first step, atomic forces and total energies of the structures were minimized with an energy cutoff of 600 eV, an electronic convergence criterion of 10^{-8}, and a force minimization criterion of 0.005 eV/Å with a single k point (Γ) using the conjugate-gradient algorithm. After obtaining a well optimized model, dynamic calculations were carried out under a harmonic approximation. The normal modes are computed by finite difference method by displacing each atom with 0.015 Å in six directions ($\pm x$, $\pm y$, $\pm z$). The VDOS is defined as

$$g(\omega) = \frac{1}{3N}\sum_{i=1}^{3N} \delta(\omega - \omega_i) \quad (4.5)$$

where $3N$ is the total number of modes with N number of atoms and ω_i is the eigenfrequency of the ith normal mode. We evaluated the VDOS by using Gaussian broadening with $\sigma = 12.0$ cm^{-1}.

Additional information can be obtained from the vibrational density of states by decomposition of total VDOS into contribution due to individual atoms. The partial VDOS can be obtained by[66]

$$g_\alpha(\omega) = \frac{1}{3N}\sum_{i=1}^{N_\alpha}\sum_n |e_i^n|^2\, \delta(\omega - \omega_n) \quad (4.6)$$

where $|e_i^n|^2$ is a square of the eigenvector, N_α is the number of atoms of α species, and $g(\omega) = \sum_\alpha g_\alpha(\omega)$. The calculated total and partial vibrational density of states calculated for three regions in the interface, crystalline, amorphous, and interfacial regions are shown in Figure 13a.

In addition to diffraction experiments, infrared (IR) spectroscopy is frequently used for material characterization. This is particularly important in order to understand the role of hydrogen in this study. An accurate *ab initio* based modeling of the vibrational, IR, and Raman spectra is key to comparing experimental observations to understand the properties of materials. IR spectroscopy can be represented by phonon density close to the Γ point, with weighted spectral lines and broadened lifetimes.[67] The absolute infrared (IR) activity is represented by the square of change in the macroscopic polarization (dipole moment per unit volume) with respect to displacement along the normal mode. The Born effective-charge tensor captures the change in polarization with respect to atomic

https://doi.org/10.1021/acsami.2c09604
ACS Appl. Mater. Interfaces XXXX, XXX, XXX−XXX

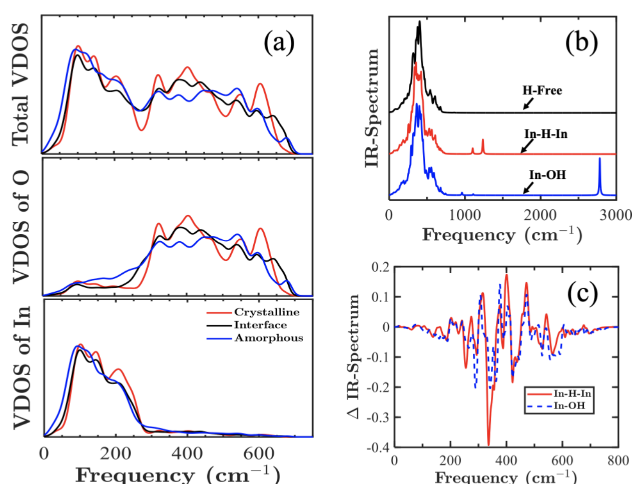

Figure 13. (a) Total and partial vibrational density of states calculated for three regions in the interface. (b) IR spectrum calculated for the fully optimized H-free interface and the structures with the lowest-energy In−OH and In−H−In defects. (c) Difference between the IR spectra of H-free and each of the H-doped cases.

displacements.[67] The calculated IR spectrum for the H-free c/a interface as well as for the structures with the In−OH and In−H−In defects that correspond to the lowest formation energy are shown in Figure 13b. Also, a difference between the IR spectra of H-free and each of the H-doped cases is calculated and shown in Figure 13c.

Finally, to study thermal stability of the several H defects, we performed molecular dynamics simulations at elevated temperatures: namely, at 100, 200, 300, 400, and 500 K. For these calculations, an energy cutoff of 400 eV, a single Γ-point method, and an integration step of 0.5 ps were employed.

■ ASSOCIATED CONTENT

Supporting Information

The Supporting Information is available free of charge at https://pubs.acs.org/doi/10.1021/acsami.2c09604.

> Comparison of the calculated inverse participation ratio and electron localization for the H-free c/a interface and several H-doped models and the calculated formation energy of charged defects in the H-doped c/a interface (PDF)

■ AUTHOR INFORMATION

Corresponding Author

Julia E. Medvedeva − *Department of Physics, Missouri University of Science & Technology, Rolla, Missouri 65409, United States;* orcid.org/0000-0001-7142-1644; Email: juliaem@mst.edu

Authors

Kapil Sharma − *Department of Physics, Missouri University of Science & Technology, Rolla, Missouri 65409, United States*

Bishal Bhattarai − *Department of Physics, Missouri University of Science & Technology, Rolla, Missouri 65409, United States;* orcid.org/0000-0002-8616-7471

Mariana I. Bertoni − *Ira A. Fulton School of Engineering, Arizona State University, Tempe, Arizona 85281, United States;* orcid.org/0000-0002-0415-837X

Complete contact information is available at: https://pubs.acs.org/10.1021/acsami.2c09604

Notes

The authors declare no competing financial interest.

■ ACKNOWLEDGMENTS

The authors acknowledge support from the National Science Foundation (NSF) DMREF program (grants DMR-1729779 and DMR-1842467) and from the Department of Energy (DOE), Office of Energy Efficiency and Renewable Energy (EERE), SETO FY20 program (grant DE-EE0009346). The computational resources were provided by Missouri S&T and by the NSF-MRI program (grant OAC-1919789).

■ REFERENCES

(1) Hallam, B. J.; Hamer, P. G.; Ciesla nee Wenham, A. M.; Chan, C. E.; Vicari Stefani, B.; Wenham, S. Development of Advanced Hydrogenation Processes for Silicon Solar Cells via an Improved Understanding of the Behaviour of Hydrogen in Silicon. *Progress in Photovoltaics: Research and Applications* **2020**, *28*, 1217−1238.

(2) Nomura, K.; Ohta, H.; Takagi, A.; Kamiya, T.; Hirano, M.; Hosono, H. Room-temperature Fabrication of Transparent Flexible Thin-film Transistors Using Amorphous Oxide Semiconductors. *Nature* **2004**, *432*, 488−492.

(3) Kamiya, T.; Nomura, K.; Hosono, H. Present Status of Amorphous In-Ga-Zn-O Thin-film Transistors. *Sci. Technol. Adv. Mater.* **2010**, *11*, 044305−044305.

(4) Park, J. S.; Maeng, W.-J.; Kim, H.-S.; Park, J.-S. Review of Recent Developments in Amorphous Oxide Semiconductor Thin-Film Transistor Devices. *Thin Solid Films* **2012**, *520*, 1679−1693.

(5) Nathan, A.; Lee, S.; Jeon, S.; Robertson, J. Amorphous Oxide Semiconductor TFTs for Displays and Imaging. *Journal of Display Technology* **2014**, *10*, 917−927.

(6) Cao, W.; Li, J.; Chen, H.; Xue, J. Transparent Electrodes for Organic Optoelectronic Devices: A Review. *Journal of Photonics for Energy* **2014**, *4*, 040990.

(7) Yu, X.; Marks, T. J.; Facchetti, A. Metal Oxides for Optoelectronic Applications. *Nat. Mater.* **2016**, *15*, 383−396.

(8) Petti, L.; Münzenrieder, N.; Vogt, C.; Faber, H.; Büthe, L.; Cantarella, G.; Bottacchi, F.; Anthopoulos, T. D.; Tröster, G. Metal Oxide Semiconductor Thin-film Transistors for Flexible Electronics. *Applied Physics Reviews* **2016**, *3*, 021303.

(9) Morales-Masis, M.; De Wolf, S.; Woods-Robinson, R.; Ager, J. W.; Ballif, C. Transparent Electrodes for Efficient Optoelectronics. *Advanced Electronic Materials* **2017**, *3*, 1600529.

(10) Coll, M. Towards Oxide Electronics: a Roadmap. *Appl. Surf. Sci.* **2019**, *482*, 1−93.

(11) Ferreira, I., et al. Role of Hydrogen Plasma on Electrical and Optical Properties of ZGO, ITO and IZO Transparent and Conductive Coatings. *Thin Solid Films* **2006**, *511−512*, 295−298.

(12) Nomura, K.; Kamiya, T.; Hosono, H. Effects of Diffusion of Hydrogen and Oxygen on Electrical Properties of Amorphous Oxide Semiconductor, In-Ga-Zn-O. *ECS Journal of Solid State Science and Technology* **2013**, *2*, P5.

(13) Lyubchyk, A.; Vicente, A.; Soule, B.; Alves, P. U.; Mateus, T.; Mendes, M. J.; Águas, H.; Fortunato, E.; Martins, R. Mapping the Electrical Properties of ZnO-Based Transparent Conductive Oxides Grown at Room Temperature and Improved by Controlled Postdeposition Annealing. *Advanced Electronic Materials* **2016**, *2*, 1500287.

(14) Bang, J.; Matsuishi, S.; Hosono, H. Hydrogen Anion and Subgap States in Amorphous In−Ga−Zn−O Thin Films for TFT Applications. *Appl. Phys. Lett.* **2017**, *110*, 232105.

(15) Gaspar, D.; Pereira, L.; Gehrke, K.; Galler, B.; Fortunato, E.; Martins, R. High Mobility Hydrogenated Zinc Oxide Thin Films. *Sol. Energy Mater. Sol. Cells* **2017**, *163*, 255−262.

(16) Kageyama, H.; Hayashi, K.; Maeda, K.; Attfield, J. P.; Hiroi, Z.; Rondinelli, J. M.; Poeppelmeier, K. R. Expanding Frontiers in Materials Chemistry and Physics with Multiple Anions. *Nat. Commun.* **2018**, *9*, 772.

(17) Mattson, G. W.; Vogt, K. T.; Wager, J. F.; Graham, M. W. Hydrogen Incorporation into Amorphous Indium Gallium Zinc Oxide Thin-film Transistors. *J. Appl. Phys.* **2022**, *131*, 105701.

(18) Van de Walle, C. G.; Neugebauer, J. Universal Alignment of Hydrogen Levels in Semiconductors, Insulators and Solutions. *Nature* **2003**, *423*, 626−628.

(19) Limpijumnong, S.; Reunchan, P.; Janotti, A.; Van de Walle, C. G. Hydrogen Doping in Indium Oxide: An Ab Initio Study. *Phys. Rev. B* **2009**, *80*, 193202.

(20) King, P. D. C.; Lichti, R. L.; Celebi, Y. G.; Gil, J. M.; Vil ao, R. C.; Alberto, H. V.; Piroto Duarte, J.; Payne, D. J.; Egdell, R. G.; McKenzie, I.; McConville, C. F.; Cox, S. F. J.; Veal, T. D. Shallow Donor State of Hydrogen in In_2O_3 and SnO_2: Implications for Conductivity in Transparent Conducting Oxides. *Phys. Rev. B* **2009**, *80*, 081201.

(21) Varley, J. B.; Peelaers, H.; Janotti, A.; Van de Walle, C. G. Hydrogenated Cation Vacancies in Semiconducting Oxides. *J. Phys.: Condens. Matter* **2011**, *23*, 334212.

(22) Meléndez, J. J.; Wierzbowska, M. In_2O_3 Doped with Hydrogen: Electronic Structure and Optical Properties from the Pseudopotential Self-interaction Corrected Density Functional Theory and the Random Phase Approximation. *J. Phys. Chem. C* **2016**, *120*, 4007−4015.

(23) Samanta, A.; Varley, J. B.; Lordi, V. Analysis of Defects in In_2O_3:H Synthesized in Presence of Water Vapor and Hydrogen Gas Mixture. *J. Appl. Phys.* **2021**, *129*, 045102.

(24) Rosén, J.; Warschkow, O. Electronic Structure of Amorphous Indium Oxide Transparent Conductors. *Phys. Rev. B* **2009**, *80*, 115215.

(25) Deng, H.-X.; Wei, S.-H.; Li, S.-S.; Li, J.; Walsh, A. Electronic Origin of the Conductivity Imbalance between Covalent and Ionic Amorphous Semiconductors. *Phys. Rev. B* **2013**, *87*, 125203.

(26) Medvedeva, J. E.; Buchholz, D. B.; Chang, R. P. Recent Advances in Understanding the Structure and Properties of Amorphous Oxide Semiconductors. *Advanced Electronic Materials* **2017**, *3*, 1700082.

(27) Medvedeva, J.; Zhuravlev, I.; Burris, C.; Buchholz, D.; Grayson, M.; Chang, R. Origin of High Carrier Concentration in Amorphous Wide-bandgap Oxides: Role of Disorder in Defect Formation and Electron Localization in In_2O_{3-x}. *J. Appl. Phys.* **2020**, *127*, 175701.

(28) Medvedeva, J. E.; Caputa-Hatley, E.; Zhuravlev, I. Metallic Networks and Hydrogen Compensation in Highly Nonstoichiometric Amorphous In_2O_{3-x}. *Phys. Rev. Materials* **2022**, *6*, 025601.

(29) Medvedeva, J. In *Amorphous Oxide Semiconductors: IGZO and Related Materials for Display and Memory*; Hosono, H., Kumomi, H., Eds.; Wiley: 2022.

(30) Koida, T.; Fujiwara, H.; Kondo, M. Hydrogen-doped In_2O_3 as High-mobility Transparent Conductive Oxide. *Jpn. J. Appl. Phys.* **2007**, *46*, L685.

(31) Koida, T.; Fujiwara, H.; Kondo, M. Structural and Electrical Properties of Hydrogen-doped In_2O_3 Films Fabricated by Solid-phase Crystallization. *J. Non-Cryst. Solids* **2008**, *354*, 2805−2808.

(32) Koida, T.; Kondo, M.; Tsutsumi, K.; Sakaguchi, A.; Suzuki, M.; Fujiwara, H. Hydrogen-doped In_2O_3 Transparent Conducting Oxide Films Prepared by Solid-phase Crystallization Method. *J. Appl. Phys.* **2010**, *107*, 033514.

(33) Macco, B.; Wu, Y.; Vanhemel, D.; Kessels, W. High Mobility In_2O_3: H Transparent Conductive Oxides Prepared by Atomic Layer Deposition and Solid Phase Crystallization. *Physica Status Solidi (RRL)−Rapid Research Letters* **2014**, *8*, 987−990.

(34) Huang, W.; et al. Experimental and Theoretical Evidence for Hydrogen Doping in Polymer Solution-processed Indium Gallium Oxide. *Proc. Natl. Acad. Sci. U. S. A.* **2020**, *117*, 18231−18239.

(35) Husein, S.; Stuckelberger, M.; West, B.; Ding, L.; Dauzou, F.; Morales-Masis, M.; Duchamp, M.; Holman, Z.; Bertoni, M. I. Carrier Scattering Mechanisms Limiting Mobility in Hydrogen-doped Indium Oxide. *J. Appl. Phys.* **2018**, *123*, 245102.

(36) Wardenga, H. F.; Frischbier, M. V.; Morales-Masis, M.; Klein, A. In Situ Hall Effect Monitoring of Vacuum Annealing of In_2O_3: H Thin Films. *Materials* **2015**, *8*, 561−574.

(37) Koida, T.; Ueno, Y.; Shibata, H. In_2O_3-based Transparent Conducting Oxide Films with High Electron Mobility Fabricated at Low Process Temperatures. *Physica Status Solidi (a)* **2018**, *215*, 1700506.

(38) Muydinov, R.; Steigert, A.; Wollgarten, M.; Michałowski, P. P.; Bloeck, U.; Pflug, A.; Erfurt, D.; Klenk, R.; Körner, S.; Lauermann, I.; Szyszka, B. Crystallisation Phenomena of In_2O_3:H Films. *Materials* **2019**, *12*, 266.

(39) Kresse, G.; Hafner, J. Ab Initio Molecular Dynamics for Liquid Metals. *Phys. Rev. B* **1993**, *47*, 558−561.

(40) Kresse, G.; Hafner, J. Ab Initio Molecular-dynamics Simulation of the Liquid-metal−amorphous-semiconductor Transition in Germanium. *Phys. Rev. B* **1994**, *49*, 14251−14269.

(41) Kresse, G.; Furthmuller, J. Efficient Iterative Schemes for Ab Initio Total-energy Calculations Using a Plane-wave Basis Set. *Phys. Rev. B* **1996**, *54*, 11169−11186.

(42) Kresse, G.; Furthmuller, J. Efficiency of Ab-initio Total Energy Calculations for Metals and Semiconductors Using a Plane-wave Basis Set. *Comput. Mater. Sci.* **1996**, *6*, 15−50.

(43) Buchholz, D. B.; Ma, Q.; Alducin, D.; Ponce, A.; Jose-Yacaman, M.; Khanal, R.; Medvedeva, J. E.; Chang, R. P. The Structure and Properties of Amorphous Indium Oxide. *Chem. Mater.* **2014**, *26*, 5401−5411.

(44) Khanal, R.; Buchholz, D. B.; Chang, R. P.; Medvedeva, J. E. Composition-dependent Structural and Transport Properties of Amorphous Transparent Conducting Oxides. *Phys. Rev. B* **2015**, *91*, 205203.

(45) Perdew, J. P.; Burke, K.; Ernzerhof, M. Generalized Gradient Approximation Made Simple. *Phys. Rev. Lett.* **1996**, *77*, 3865−3868.

(46) Perdew, J. P.; Burke, K.; Ernzerhof, M. Generalized Gradient Approximation Made Simple [Phys. Rev. Lett. 77, 3865 (1996)]. *Phys. Rev. Lett.* **1997**, *78*, 1396−1396.

(47) Heyd, J.; Scuseria, G. E.; Ernzerhof, M. Hybrid Functionals Based on a Screened Coulomb Potential. *J. Chem. Phys.* **2003**, *118*, 8207−8215.

(48) Heyd, J.; Peralta, J. E.; Scuseria, G. E.; Martin, R. L. Energy Band Gaps and Lattice Parameters Evaluated with the Heyd-Scuseria-Ernzerhof Screened Hybrid Functional. *J. Chem. Phys.* **2005**, *123*, 174101.

(49) Medvedeva, J. E.; Bhattarai, B. Hydrogen Doping in Wide-bandgap Amorphous In−Ga−O Semiconductors. *Journal of Materials Chemistry C* **2020**, *8*, 15436−15449.

(50) Walsh, A.; Da Silva, J. L. F.; Wei, S.-H. Interplay between Order and Disorder in the High Performance of Amorphous Transparent Conducting Oxides. *Chem. Mater.* **2009**, *21*, 5119−5124.

(51) Husein, S.; Medvedeva, J. E.; Perkins, J. D.; Bertoni, M. I. The Role of Cation Coordination in the Electrical and Optical Properties of Amorphous Transparent Conducting Oxides. *Chem. Mater.* **2020**, *32*, 6444−6455.

(52) Jia, J.; Iwasaki, S.; Yamamoto, S.; Nakamura, S.-i.; Magome, E.; Okajima, T.; Shigesato, Y. Temporal Evolution of Microscopic Structure and Functionality during Crystallization of Amorphous Indium-Based Oxide Films. *ACS Appl. Mater. Interfaces* **2021**, *13*, 31825−31834. PMID: 34191476

(53) Tang, H.; Kishida, Y.; Ide, K.; Toda, Y.; Hiramatsu, H.; Matsuishi, S.; Ueda, S.; Ohashi, N.; Kumomi, H.; Hosono, H.; Kamiya, T. Multiple Roles of Hydrogen Treatments in Amorphous In−Ga−Zn−O Films. *ECS Journal of Solid State Science and Technology* **2017**, *6*, P365−P372.

(54) Sallis, S.; Butler, K. T.; Quackenbush, N. F.; Williams, D. S.; Junda, M.; Fischer, D. A.; Woicik, J. C.; Podraza, N. J.; White, B. E.; Walsh, A.; Piper, L. F. J. Origin of Deep Subgap States in Amorphous Indium Gallium Zinc Oxide: Chemically Disordered Coordination of Oxygen. *Appl. Phys. Lett.* **2014**, *104*, 232108.

https://doi.org/10.1021/acsami.2c09604
ACS Appl. Mater. Interfaces XXXX, XXX, XXX−XXX

(55) Ide, K.; Nomura, K.; Hosono, H.; Kamiya, T. Electronic Defects in Amorphous Oxide Semiconductors: A Review. *Physica Status Solidi (a)* **2019**, *216*, 1800372.

(56) Moffitt, S. L.; Zhu, Q.; Ma, Q.; Falduto, A. F.; Buchholz, D. B.; Chang, R. P. H.; Mason, T. O.; Medvedeva, J. E.; Marks, T. J.; Bedzyk, M. J. Probing the Unique Role of Gallium in Amorphous Oxide Semiconductors through Structure-Property Relationships. *Advanced Electronic Materials* **2017**, *3*, 1700189.

(57) Rucavado, E.; Landucci, F.; Döbeli, M.; Jeangros, Q.; Boccard, M.; Hessler-Wyser, A.; Ballif, C.; Morales-Masis, M. Zr-doped Indium Oxide Electrodes: Annealing and Thickness Effects on Microstructure and Carrier Transport. *Phys. Rev. Materials* **2019**, *3*, 084608.

(58) Marsillac, S.; Combot-Marie, A.; Bernède, J.; Conan, A. Experimental Evidence of the Low-temperature Formation of γ-In_2Se_3 Thin Films Obtained by a Solid-state Reaction. *Thin Solid Films* **1996**, *288*, 14−20.

(59) Hohenberg, P.; Kohn, W. Inhomogeneous Electron Gas. *Phyical Review* **1964**, *136*, B864−B871.

(60) Kohn, W.; Sham, L. J. Self-Consistent Equations Including Exchange and Correlation Effects. *Phys. Rev.* **1965**, *140*, A1133−A1138.

(61) Blochl, P. E. Projector Augmented-wave Method. *Phys. Rev. B* **1994**, *50*, 17953−17979.

(62) Kresse, G.; Joubert, D. From Ultrasoft Pseudopotentials to the Projector Augmented-wave Method. *Phys. Rev. B* **1999**, *59*, 1758−1775.

(63) Hoppe, R.; Voigt, S.; Glaum, H.; Kissel, J.; Muller, H. P.; Bernet, K. A New Route to Charge Distributions in Ionic Solids. *Journal of the Less Common Metals* **1989**, *156*, 105−122.

(64) Tang, W.; Sanville, E.; Henkelman, G. A Grid-based Bader Analysis Algorithm without Lattice Bias. *J. Phys.: Condens. Matter* **2009**, *21*, 084204.

(65) Momma, K.; Izumi, F. VESTA 3 for Three-dimensional Visualization of Crystal, Volumetric and Morphology data. *J. Appl. Crystallogr.* **2011**, *44*, 1272−1276.

(66) Pasquarello, A.; Sarnthein, J.; Car, R. Dynamic Structure Factor of Vitreous Silica from First Principles: Comparison to Neutron-inelastic-scattering Experiments. *Phys. Rev. B* **1998**, *57*, 14133−14140.

(67) Skelton, J. M.; Burton, L. A.; Jackson, A. J.; Oba, F.; Parker, S. C.; Walsh, A. Lattice Dynamics of the Tin Sulphides SnS_2, SnS and Sn_2S_3: Vibrational Spectra and Thermal Transport. *Phys. Chem. Chem. Phys.* **2017**, *19*, 12452−12465.

https://doi.org/10.1021/acsami.2c09604
ACS Appl. Mater. Interfaces XXXX, XXX, XXX−XXX